**Li, Liang and Cheng, Zhengshun and Yuan, Zhiming and Gao, Yan (2018) Short-term extreme response and fatigue damage of an integrated offshore renewable energy system. Renewable Energy, 126. pp. 617-629. ISSN 0960-1481 , http://dx.doi.org/10.1016/j.renene.2018.03.087**

# Short-term extreme response and fatigue damage of an integrated offshore renewable energy system

Liang Li[a], Zhengshun Cheng[b], Zhiming Yuan[a, *], Yan Gao[a]

[a] Department of Naval Architecture, Ocean and Marine Engineering, University of Strathclyde, 100 Montrose Street, Glasgow, G4 0LZ, UK

[b] Department of Marine Technology and Centre for Autonomous Marine Operations and Systems, Norwegian University of Science and Technology (NTNU), Trondheim, NO-7491, Norway

[*]Corresponding author: zhiming.yuan@strath.ac.uk (Z-M. Yuan).

## Abstract

This study addresses short-term extreme response and fatigue damage of an integrated wind, wave and tidal energy system. The integrated concept is based on the combination of a spar type floating wind turbine, a wave energy converter and two tidal turbines. Aero-hydro-mooring coupled analysis is performed in time-domain to capture the dynamic response of the combined concept in a set of environmental conditions. The mean up-crossing rate method is used to evaluate the extreme response, which takes advantage of an extrapolation method to reduce the simulation sample size. The cumulative fatigue damage is computed based on the S-N method. Simulation results show that the tower base fore-aft bending moment is improved, in terms of extreme value and fatigue damage. Nevertheless, the tension force of a mooring line is worsened. The mooring line bears increased maximum tension due to the tidal turbine thrust force and it is subjected to higher fatigue damage load as well.

Keyword: extreme response, fatigue damage, renewable energy, floating wind turbine, wave energy converter, tidal turbine

## 1. Introduction

With expanding global demand for power and increasing public awareness to sustainable development, great efforts are taken to exploit the offshore renewable energy resources and a set of offshore renewable energy devices are developed. Statoil launched a demo project of a spar type offshore floating wind turbine, namely the Hywind concept, which is the first full scale floating wind turbine that has ever been built [1]. Principle Power installed a full scale 2MW WindFloat prototype near the coast of Portugal [2]. At the same time, researchers across the world are working on the numerical and experimental studies of floating wind turbine [3-8]. Apart from floating wind turbine, wave energy converter (WEC) and tidal turbine are also widely used to harvest energy from the ocean. Zhang and Yang [9] captured the power output of an oscillating-body WEC. Two symmetrically oblique springs and a linear damper were applied to model the nonlinear behaviour of the power take off (PTO) system. Elhanafi et al. [10] tested the hydrodynamic performance of a floating-moored WEC in regular and irregular waves with both experimental and numerical methods. Ning et al. [11] . investigated the dynamics of a fixed oscillating-water-column WEC in a set of environmental conditions. A critical wave slope was identified in which the efficiency reaches the maximum. The full wake structure of a horizontal tidal turbine was experimentally studied by Chen et al. [12] . Lo Brutto et al. [13] developed a semi-analytic method to optimize the layout of tidal farms, which aimed to maximum the total power production.

Currently, producing power from a single type of ocean energy resource is facing the challenges of high cost and low harvesting efficiency. Therefore, the concept of offshore integrated renewable energy system is developed to address these issues. Aubault et al. [14] incorporated an oscillating-water-column WEC into a semi-submersible floating wind turbine. They showed that the overall cost could be reduced by sharing the mooring system and the power infrastructure. Muliawan et al. [15] studied the dynamic response and the power performance of the so-called STC (Spar-Torus Combination) concept in various operational conditions. Their simulation results revealed a synergy between wind and wave energy generation. Experimental and numerical studies of the STC in survival mode were conducted by Wang et al. [16]. Michailides et al. [17] incorporated a flap-type WEC to a semi-submersible floating wind turbine and investigated the effect of WECs on the response of the integrated system. Their study showed that the combined operation of the rotating flaps resulted in an increase of the produced power without affecting the critical response quantities of the semi-submersible platform significantly. Li et al. [18] proposed a hybrid offshore renewable energy device by combine a floating wind turbine, a WEC and two tidal turbines. It was shown that the overall power production was increased while the platform motions were reduced. Bachynski and Moan [19] studied the effects of three point-absorber WECs on a TLP (tension leg platform) floating wind turbine in operational and 50-year extreme environmental conditions, in terms of power production, structural loads and platform motions.

In practice, the ultimate limit state and fatigue limit state are essential items in the design of an offshore renewable energy device. Cheng et al. [20] compared the extreme structural response and fatigue damage of a horizontal axis floating wind turbine and a vertical axis floating wind turbine. Hu et al. [21] developed an integrated structural strength analysis method for a spar type floating wind turbine. Inertia and wave-induced loads were addressed with a quasi-static method and the wind force was dealt with a static approach. Li et al. [22] discussed the limitation of original environmental contour method in the application to offshore wind turbines. A modified approach was proposed and they showed that the predicted results were close to full long-term analysis. Michailides et al. [23] examined the response of a combined wind/wave energy concept in extreme environmental conditions with both experimental and numerical methods. Liu et al. [24] studied the aerodynamic damping effect on offshore wind turbine tower fatigue loads and different aerodynamic damping models were used. Aggarwal et al. [25] studied the nonlinear short-term extreme responses of a spar type floating wind turbine. Li et al. [26] investigated the fatigue analysis for tower base of a spar-type wind turbine. The effects of simulation length, wind-wave misalignment on the fatigue damage were studied. Marino et al. [27] investigated the fatigue loads of a floating wind turbine with both linear and nonlinear wave models. Graf et al. [28] used the Monte Carlo approach to evaluate the long-term fatigue loads of a floating wind turbine. They found that this approach significantly increased the computational efficiency but the effectiveness was reduced as nonlinearity effect became important.

This work is the second part of the investigation on an integrated wind, wave and tidal energy system. In previous study [18], platform motions and power production of the hybrid device were simulated and comparisons were made with a spar type floating wind turbine. It was shown that the overall power production was enhanced and surge and pitch motions of the platform were reduced at the same time. Nevertheless, the hybrid system gave a worsened heave motion. This study will examine the short-term extreme structural response and fatigue damage of the integrated concept in a wide range of environmental conditions. The mean-up crossing rate method is used to evaluate the extreme response and the fatigue damage is estimated with the S-N approach. The analysis results will be compared with those of a spar type floating wind turbine to clarify the effect of the WEC and the tidal turbines.

# 2. Model description.

The hybrid concept addressed in this study, namely 'HWNC (Hywind-Wavebob-NACA Combination)' [18] (see Fig. 1), is inspired by the spar type floating wind turbine Hywind [29], the two-body floating WEC 'Wavebob' and the tidal turbines with the NACA 638xx aerofoil series. The WEC, designed to move only in heave mode relative to the platform while no relative surge, sway, roll, pitch and yaw motions are allowed, is connected to the platform through mechanical facilities. Two tidal turbines are installed to harvest energy from the sea current. The main dimensions of the HWNC are presented in Table 1 and the inertial properties of each component are listed in Table 2.

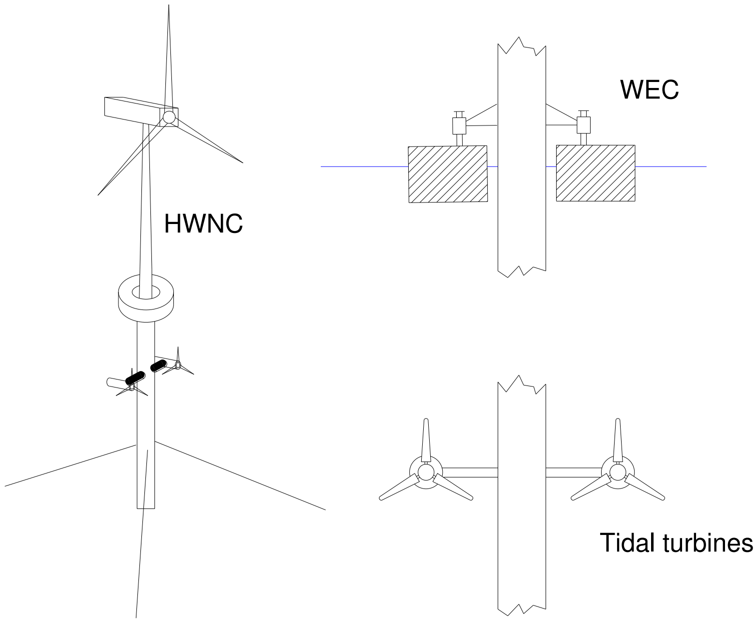


Fig. 1. HWNC concept.

Table 1
Main dimensions of the HWNC.

| | Item | Value |
|---|---|---|
| Platform | Draft | 120 m |
| | Tower base above still water level (SWL) | 10 m |
| | Depth to top of taper below SWL | 4 m |
| | Depth to bottom of taper below SWL | 12 m |
| | Platform diameter above taper | 6.5 m |
| | Platform diameter below taper | 9.4 m |
| WEC | Draft | 4 m |
| | Outer diameter | 20 m |
| | Inner diameter | 10 m |
| Tidal turbine | Depth below SWL | 46.5 m |
| | Rotor diameter | 10 m |

Table 2
Inertial properties of subsystem.

| | Item | Value |
|---|---|---|
| Platform (with tidal turbines) | Total mass | 6,995,130 kg |
| | Centre of mass (CM) below SWL | 89.9 m |
| | Roll inertia about CM | 4,229,230,000 kg·m$^2$ |
| | Pitch inertia about CM | 4,229,230,000 kg·m$^2$ |
| | Yaw inertia about CM | 164,230,000 kg·m$^2$ |
| WEC | Total mass | 1,442,000 kg |
| | CM below SWL | 0 m |
| | Roll inertia about CM | 3,139,900 kg·m$^2$ |
| | Pitch inertia about CM | 3,139,900 kg·m$^2$ |
| | Yaw inertia about CM | 6,022,200 kg·m$^2$ |

The HWNC is operated at sea site with a water depth of 320 m and moored by three slack catenary lines. The fairleads are connected to the platform at 70 m below the still water level. Fig. 2 displays the configuration of the mooring system. Three lines are oriented at 60°, 180°, and 300° about the vertical axis. The relevant properties of the mooring lines are listed in Table 3.

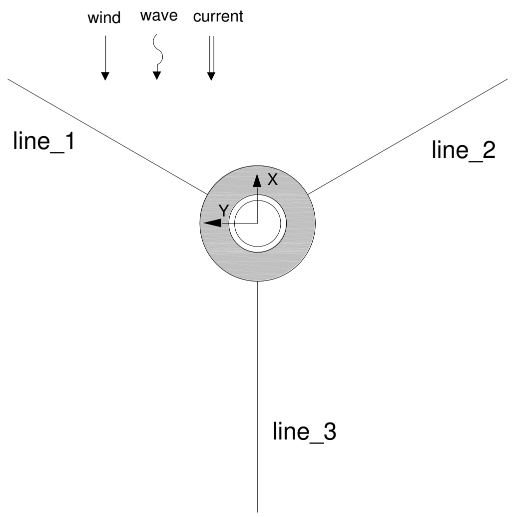


Fig. 2. Configuration of mooring lines.

Table 3
Mooring line properties.

| Item | Value |
|---|---|
| Depth to anchors | 320 m |
| Depth of fairleads | 70 m |
| Radius to anchors | 853.87 m |
| Radius to fairleads | 5.2 m |
| Unstretched mooring line length | 902.2 m |
| Mooring line diameter | 0.09 m |
| Equivalent mooring line mass density | 77.7066 kg/m |
| Equivalent mooring line extensional stiffness | 384,243,000 N |
| Additional yaw stiffness | 98,340,000 Nm/rad |

# 3. Analysis methodology

## 3.1. Aero-hydro coupled analysis

The numerical code used to perform the coupled simulation in this work is based on the combination of WindSloke developed by Li et al. [4] and WEC-Sim [30] developed under the collaboration between the National Renewable Energy Laboratory (NREL) and the Sandia National Laboratories. The aerodynamic module of WindSloke is used in this work to calculate the unsteady wind turbine thrust force by a modified blade element momentum (BEM) method. The tidal turbine thrust force is computed with the same approach. The unsteadies of the inflow caused by platform motions is considered with a dynamic wake model [31]. WEC-Sim is a wave energy converter simulation tool with the ability to model offshore systems that are comprised of rigid bodies, PTO systems and mooring systems. WEC-Sim computes the hydrodynamic forces acting on the floating bodies based on the combination of potential flow theory and Morison equation.

Three rigid bodies are established in the numerical model of the HWNC. The spar platform (with tidal turbines) and the WEC are treated as two independent floating bodies and their hydrodynamic interactions are considered. The two components are connected by the PTO facility, which is numerically treated as a spring & damper system. The stiffness coefficient K is set to 5 kN and the damping coefficient B is set to 80 kN·s/m. The wind turbine is regarded as a non-hydro body, which is rigidly mounted on the platform. Please note that deflection of the tower is not considered in this study. The mooring line is modelled with the lumped-mass approach, which divides the mooring line into a series of evenly-sized segment represented by connected nodes and spring & damper systems. The lumped-mass approach merely models the axial properties of the mooring lines while the torsional and bending properties are neglected. The effects of wave kinematics and any other external loads on the lines are also ignored in the lumped-mas model.

## 3.2. Extreme load estimation

The extreme values of stochastic responses are estimated based on the mean up-crossing rate method [32]. In an arbitrary time interval T, it can be assumed that the random number of up-crossing is approximated by Poisson distribution on condition that the up-crossing is statistically independent. This assumption is valid if the response process is not narrow banded. Once a level $y_0$ is selected, the distribution of extreme value $y_{max}$ for a random signal y(t) is described as

$$P(y_{max} \le y_0) = \exp\left(-\int_0^T v^+(y_0,t)dt\right) \tag{1}$$

where $v^+(y_0,t)$ is the up-crossing rate corresponding to level $y_0$, which denotes the instantaneous frequency of the positive slop crossings of the defined level. In this circumstance, the probability of $y_{max}$ exceeding a defined level $y_0$ is given by

$$\begin{aligned} P(y_{max} > y_0) &= 1-\exp\left(-\hat{v}^+(y_0)T\right) \\ \hat{v}^+(y_0) &= \frac{1}{T}\int_0^T v^+(y_0,t)dt \end{aligned} \tag{2}$$

The mean up-crossing rate $\hat{v}^+(y_0)$ can be easily obtained from the time series of the signal that is going to be analysed. For example, if we have k independent realizations of the random process and let $n_j^+(y_0,T)$ denote the number of up-crossings in realization j, then the sample-based mean up-crossing rate is given by

$$\begin{aligned} \hat{v}^+(y_o) &\approx \overline{v}^+(y_o) \\ \overline{v}^+(y_o) &= \frac{1}{kT}\sum_{j=1}^{k} n_j^+(y_0,T) \end{aligned} \tag{3}$$

Eq. (3) is the basic formula to approximate the mean up-crossing rate $\hat{v}^+(y_0)$ through numerical simulations. If the defined level $y_0$ is not very high, then just a few simulation realizations of the random process will produce satisfactory approximation. Nevertheless, extensive simulations are required to evaluate the extreme values in the tail region. To save computation resources, the extrapolation method proposed by Naess and Gaidai [33] is used in this study to predict the mean up-crossing rate corresponding to high level $y_0$.

The extrapolation method is based on the observation of marine structures so that it is applicable in this study. The mean up-crossing rate is approximated by

$$\begin{aligned} &\bar{v}^{+}(y) \approx v_{fit}^{+}(y) \\ &v_{fit}^{+}(y) = q \cdot \exp\left\{-a(y-b)^{c}\right\}, y \geq y_0 \end{aligned} \tag{4}$$

where q, a, b and c are all constant values. In the work of Naess and Gaidai [33], the first procedure is to determine the value of q. Afterwards, it is easy to find that plotting log|log($v_{fit}^{+}/q$)| versus log(y-b) exhibits a linear tail behaviour. Fig. 3 shows the extrapolation of mean up-crossing rate, which can approximates the mean up-crossing fairly well at low defined level $y_0$. Nevertheless, $\bar{v}^{+}$ becomes unstable in the tail region as the sample size (10 independent simulation realizations in this study) is sufficient to produce reliable results. Therefore, the fitted up-crossing rate $v_{fit}^{+}$ is used in the following part of this paper to represent the extreme responses in the tail region.

A method to examine whether the sample size is sufficient to extrapolate the up-crossing rate is to check the 95% confidence interval CI

$$\begin{aligned} &CI_{\pm}(y_o) = \bar{v}^{+}(y_o) \pm 1.96 \cdot \frac{\sigma(y_o)}{\sqrt{k}} \\ &\sigma(y_o)^2 = \frac{1}{k-1}\sum_{j=1}^{k}\left(\frac{n_j^{+}(y_0,T)}{T} - \bar{v}^{+}(y_o)\right)^2 \end{aligned} \tag{5}$$

The confidence interval obtained with 10 simulation realizations is displayed in Fig. 3. As shown, the accuracy is acceptable. 10 simulation realizations are collected to extrapolate the up-crossing rate in the following part of this paper.

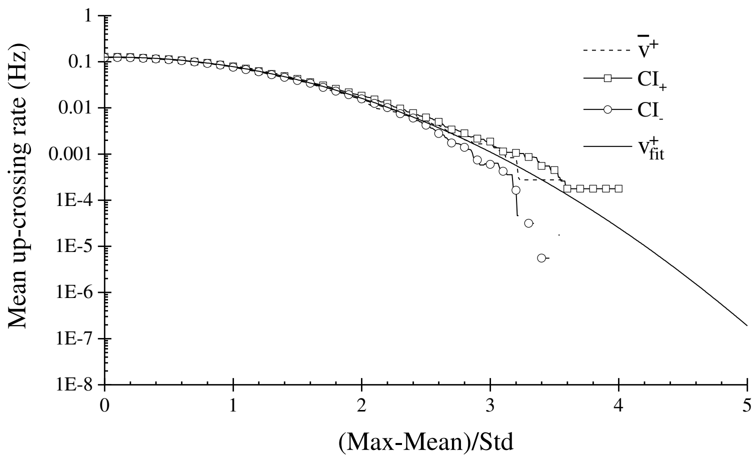


Fig. 3. Extrapolation of mean up-crossing rate of the tower base fore-aft bending moment in LC2.

### 3.3. Fatigue damage estimation

The short-term fatigue analysis is performed with MLife [34]. Wind, wave and inertial loads applied at certain structural components will cause fluctuation which will lead to fatigue damages. S-N method is used to evaluate the fatigue damages caused by these fluctuating loads. The fluctuating loads are broken down into individual hysteresis cycles by matching local minima with local maxima in the time series, which are characterized by a load-mean and range. It is assumed that the damage accumulates linearly with each of these cycles according to Miner's Rule. In this case, the overall damage rate produced by all the cycles is given by

$$\begin{gathered} DR = \sum_i \frac{n_i}{N_i(L_i^{RF})} / T \\ N_i(L_i^{RF}) = \left( 2 \cdot \frac{L^{ult} - \left| L^{MF} \right|}{\left( L_i^{RF} \right)} \right)^m \end{gathered} \tag{6}$$

$n_i$ is the damage count, $N_i$ is the number of cycles to failure, $L_i^{RF}$ is the cycle's load range corresponding to the fixed load-mean $L^{MF}$, $L^{ult}$ is the design ultimate load and m is the Wholer exponent. In this study, the design ultimate load for tower base fore-aft bending moment and mooring line tension is 680,000 kN·m and 2550 kN, respectively. The value of m is based on DNV design standard [35]. Considering the shape of the tower base and mooring line, the B1 S-N curve is selected. Afterwards, the 'air' category and 'sea water' category is selected for the tower base fore-aft bending moment and the mooring line tension, respectively. Consequently, m = 4 selected for both fore-aft bending moment and tension force. T is the simulation time length.

# 4. Validation

### 4.1. Aerodynamics validation

Since the thrust forces acting on the wind turbine and the tidal turbines are simulated with the same approach, only aerodynamic force is validated here. Firstly, the steady aerodynamic performance of the wind turbine is simulated. Fig. 4 displays the steady aerodynamic performance of the wind turbine, in terms of thrust force and rotor power output. As shown, a good agreement with the designed value [36] is reached. It should be noted that the rated rotor power output of the NREL 5WM baseline wind turbine is 5.3 WM (The rated generator power output is 5MW).

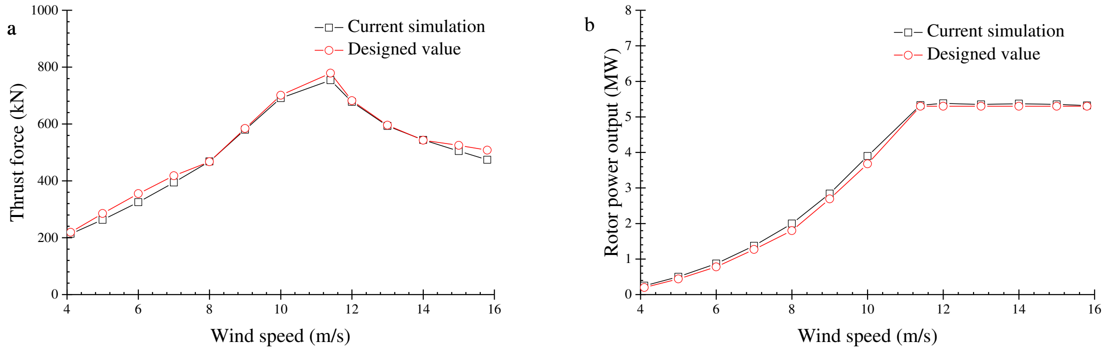


Fig. 4. Aerodynamic performance of the wind turbine. (a) thrust force; (b) rotor power output.

For a floating wind turbine, the wind force acting on the rotor is unsteady due to platform motions. To validate the unsteady aerodynamic performance, the wind turbine thrust force is simulated under a set of sinusoidal winds and the simulation results are compared with those obtained by FAST [37]. The speed of sinusoidal wind is defined as

$$V(t) = V_0 + \sin(\omega t) \tag{7}$$

where $V_0$ is the mean wind speed and $\omega$ is the varying frequency. Fig. 5 displays time series of the unsteady wind turbine thrust forces predicted by the simulation tool and FAST. The agreement with FAST is satisfactory.

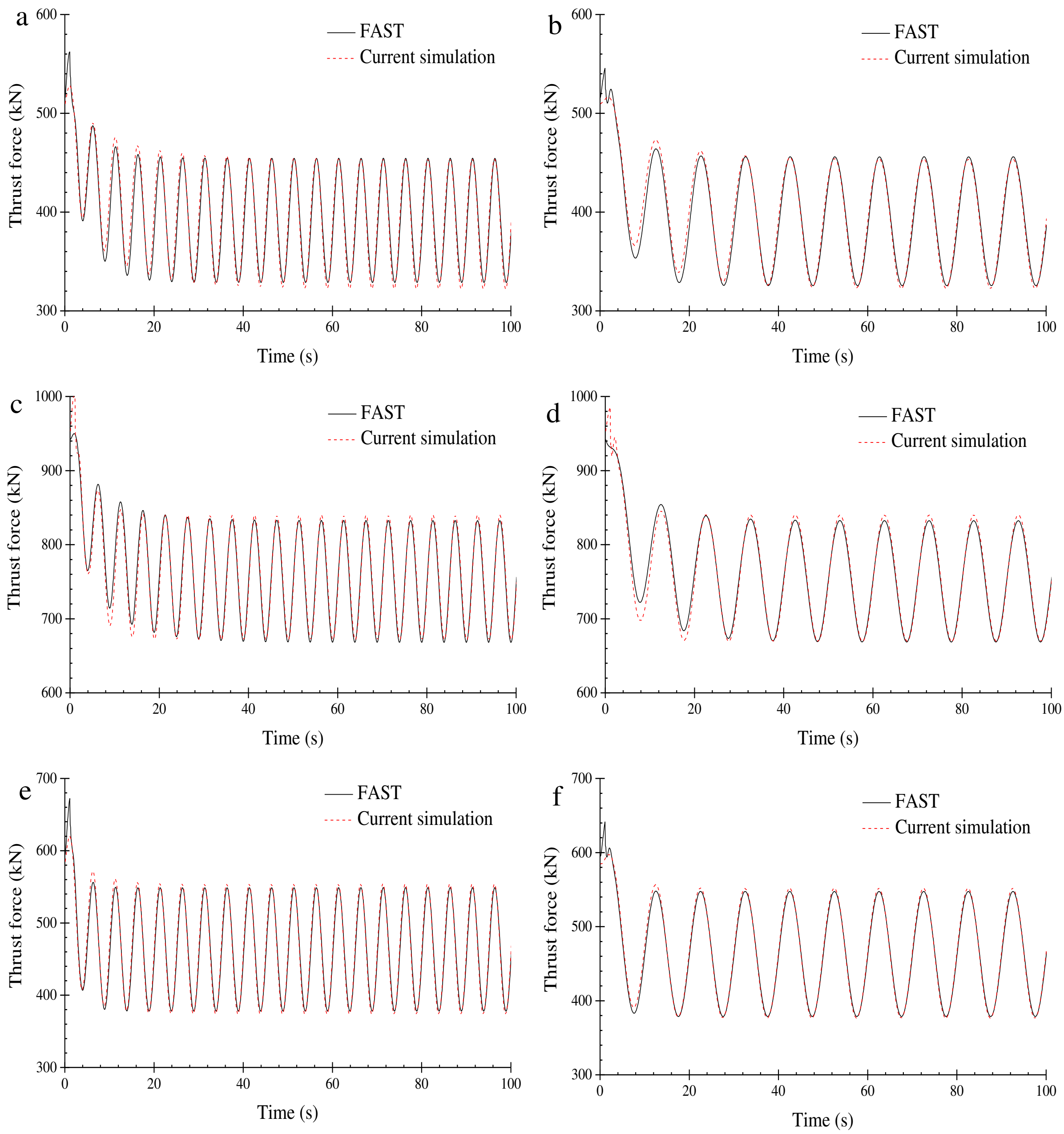


Fig. 5. Times series of unsteady wind turbine thrust forces. (a) $V_0$= 8 m/s, $\omega$ = 1.26 rad/s; (b) $V_0$ = 8 m/s, $\omega$ = 0.63rad/s; (c) $V_0$ = 11.4 m/s, $\omega$ = 1.26 rad/s; (d) $V_0$ = 11.4 m/s, $\omega$ = 0.63 rad/s; (e) $V_0$ = 14 m/s, $\omega$ = 1.26 rad/s; (f) $V_0$ = 14 m/s, $\omega$ = 0.63 rad/s.

## 4.2. Aero-hydro-mooring validation

The model test of a spar type floating wind turbine conducted by Koo et al. [38] is used to validate the numerical modelling of platform-wind turbine couplings. The spar type floating wind has an identical platform geometry with the Hywind, despite that the mass and inertia of the platform were changed. Please refer to [38] for more details of the model test set-up. White noise waves were generated in the model test to get the response amplitude operator (RAO) of platform motions in the presence of rated wind turbine thrust force. The same procedure is employed in the numerical simulation. Fig. 6 compares the RAOs acquired by the simulation tool and the experiment.

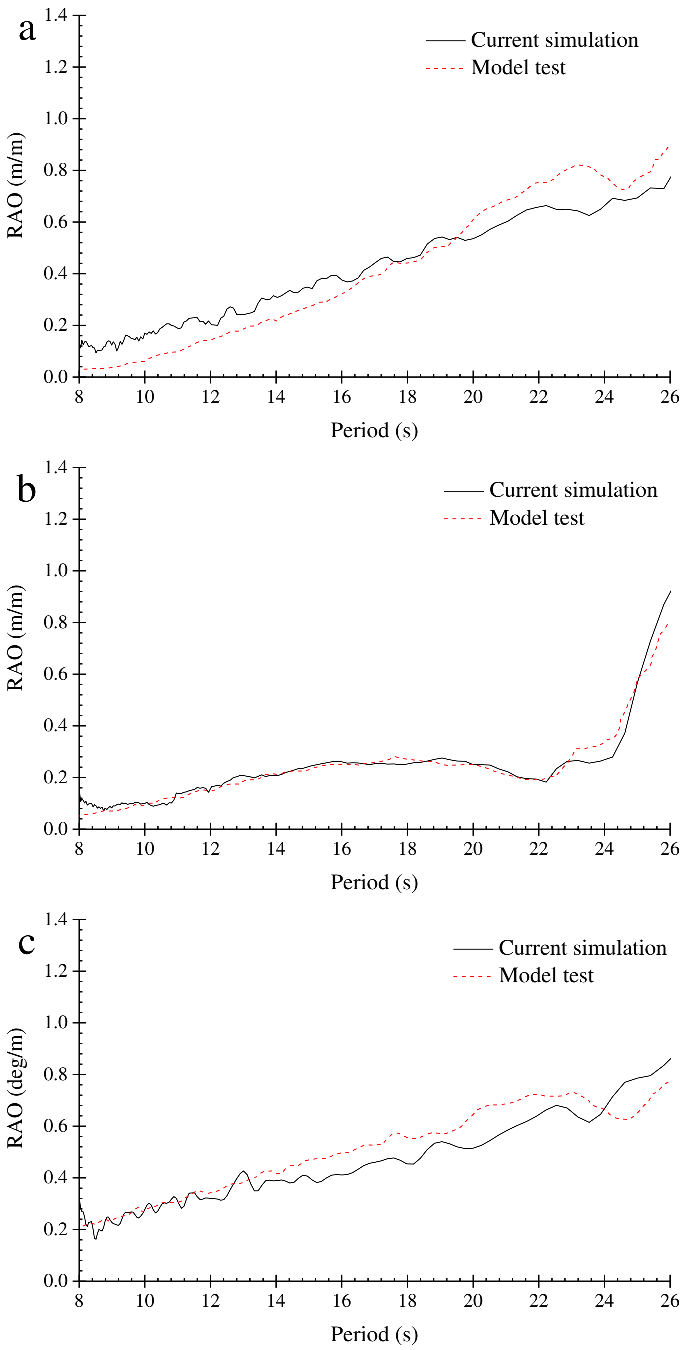


Fig. 6. RAOs of platform motions. (a) surge motion; (b) heave motion; (c) pitch motion.

# 5. Environmental conditions and Load cases

In a realistic sea site, the wind and the wave are correlated. The selection of environmental conditions is based on the joint probabilistic model of mean wind speed $U_w$ at 10 m above the mean sea level, significant wave height $H_s$ and peak period $T_p$ that proposed by Johannessen et al. [39]. It is a pity that the tidal speed is not included in the joint model so that it is set to 1 m/s in all load cases. Firstly, the mean wind speed $U_w$ is chosen. Subsequently, the fitting curve provided in [39] is used to acquire the mean significant wave height corresponding to a given mean wind speed. Finally, the mean peak period at given $U_w$ and $H_s$ is determined according to Eq. (8). The environmental condition considered in this study are listed in Table 4. Steady wind field without consideration of turbulence is adopted in all simulation cases.

$$T_p = (4.883 + 2.68 \cdot H_s^{0.529}) \cdot \left[ 1 - 0.19 \cdot \left( \frac{U_w - (1.764 + 3.426 \cdot H_s^{0.78})}{1.764 + 3.426 \cdot H_s^{0.78}} \right) \right] \tag{8}$$

Table 4
Environmental conditions.

| | $U_w$ (m/s) | $U_{hub\ height}$ (m/s) | $H_s$ (m) | $T_p$ (s) | Tidal stream speed (m/s) |
|---|---|---|---|---|---|
| LC1 | 5 | 6.8 | 2.38 | 9.84 | 1 |
| LC2 | 8 | 10.8 | 3.13 | 10.17 | 1 |
| LC3 | 10 | 13.6 | 3.55 | 10.29 | 1 |
| LC4 | 12 | 16.3 | 4.17 | 10.62 | 1 |
| LC5 | 14 | 19.0 | 4.75 | 10.89 | 1 |

The wind speed varies with height implying that the blades are subjected to time-varying inflow due to rotor rotation. A power law is used to estimate the wind profile U(z) at the height of z above the mean sea level (see Fig. 7)

$$U(z) = U_w \left( \frac{z}{10} \right)^{\alpha} \tag{9}$$

$\alpha$ is the power law exponent which is selected to be 0.14 according to IEC 614000-3 [40].

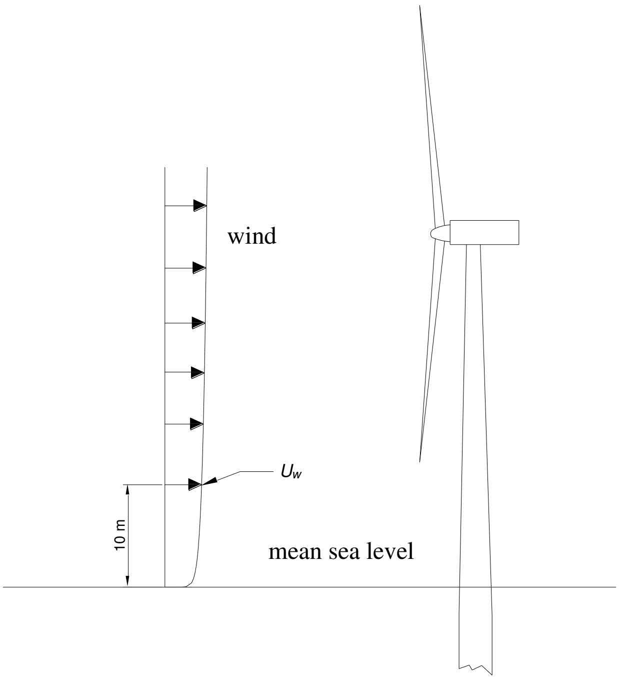


Fig. 7. Wind profile.

In each simulation case, the stochastic wave elevations are pre-generated and input to the HWNC and the Hywind respectively to ensure a reasonable comparison between the two systems. A linear wave model is adopted to generate the stochastic wave elevations, which consists of a set of regular waves with different oscillating frequency

$$\eta(t) = \sum_{j=1}^{N} A_j \cos(2\pi f_j t + \varepsilon_j)$$
$$A_j = \sqrt{2S(f_j)\Delta f} \tag{10}$$

where $A_j$, $f_j$ and $\varepsilon_j$ are the wave amplitude, frequency and random phase of the regular wave component j. S(f) is the JONSWAP wave spectrum. If $f_j$ is uniformly distributed over the wave frequency range, the stochastic wave elevations will start to repeat after a certain time interval [41]. Apparently, it has a substantial influence on the statistics of the stochastic responses, especially the prediction of the extreme values. To address this issue, the correct method used in [4] is adopted here. The wave frequency range is firstly uniformly divided in to N segments and $f_j$ is randomly distributed within segment j (see Fig. 8). The stochastic wave elevations corresponding to a specific load case are independently realized ten times. Then the ten sets of simulation results are collected to extrapolate the mean up-crossing rate and evaluate the extreme responses according to the procedures in Section 3.2.


Fig. 8. Random distribution of wave frequency.

# 6. Simulation results

The responses of the HWNC subjected to various environmental excitations are simulated. Comparisons will be made against the Hywind to demonstrate whether the installation of the WEC and the tidal turbines can improve the performance of the HWNC. 1-hr extreme response and fatigue damage are investigated. The total simulation length is set to 4000 s and only data of the last 3600 s will be collected to get rid of the transient effects arising in the initial simulation stage. A ramp function $R_f$ is also added to eliminate the transient effects

$$R_f = \begin{cases} (1+\cos(\pi + \pi t / t_r))/2 & t < t_r \\ 1 & t \geq t_r \end{cases} \tag{11}$$

where $t_r$ is the ramp time.

## 6.1. Power production and platform motions

The power production is firstly investigated. Fig. 9 displays the time series of power production of the HWNC. As shown, the contribution from the WEC and the tidal turbines are remarkable. Since the tidal turbines are installed close to the CoG of the platform, surge-pitch coupling is not significant and therefore the power output of the tidal turbines are very stable.

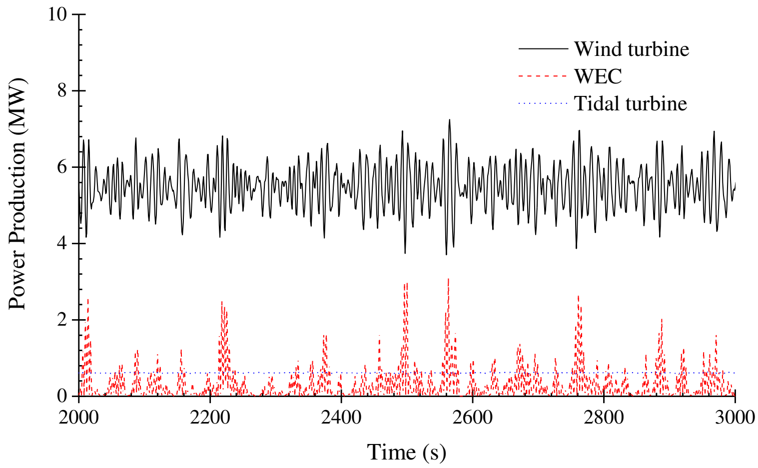


Fig. 9. Time series of power production, LC3.

The mean power production of the HWNC and the Hywind in various load cases are shown in Fig. 10. Generally, the HWNC produces approximately 25% more power than the Hywind and this percentage is even higher in below-rated operational condition. Fig. 11 compares the standard deviation of wind turbine power production. The standard deviation of the HWNC is lower than that of the Hywind, regardless of environmental conditions. It implies that the wind turbine power output is more stable with the WEC and the tidal turbines, which is obviously beneficial to the net grid.

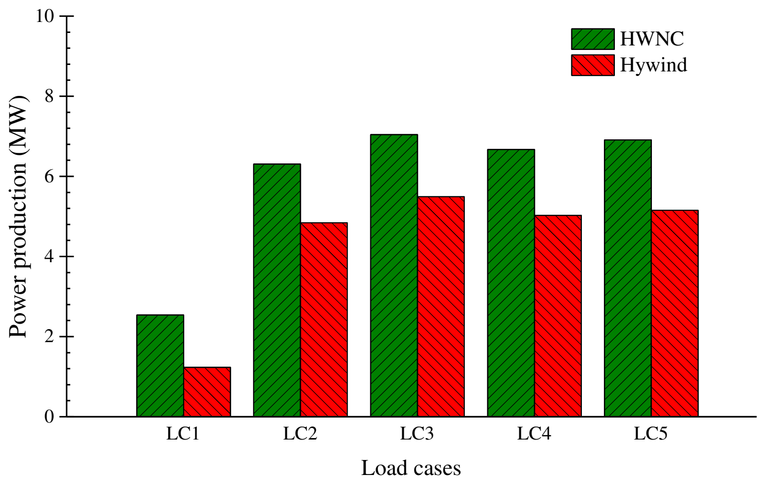


Fig. 10. Mean value of overall power production.

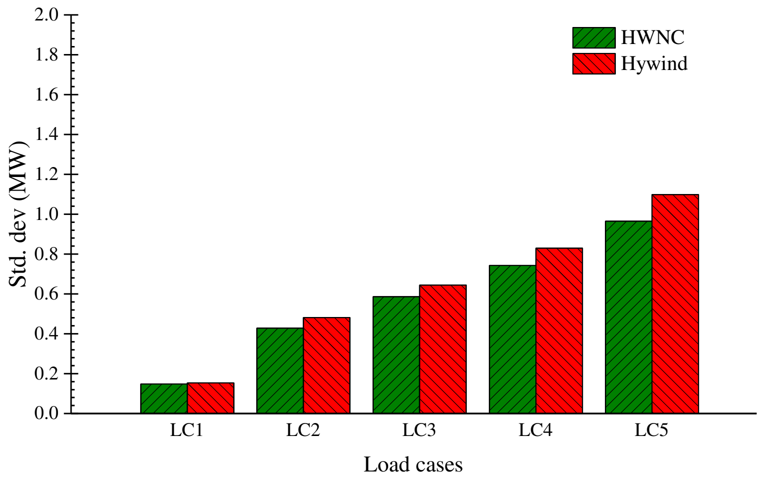


Fig. 11. Standard deviation of wind turbine power production.

Fig. 12 plots the time series of platform motions and Table 5 summarises the statistics. It is desirable to see that the surge and pitch motions are reduced. Nevertheless, the mean pitch and surge position is pushed further away from the initial equilibrium position due to the extra thrust force on the tidal turbines. It inherently implies that the mooring lines will bear more loads. Also, the heave response of the HWNC is excited considerably, much stronger than that of the Hywind.

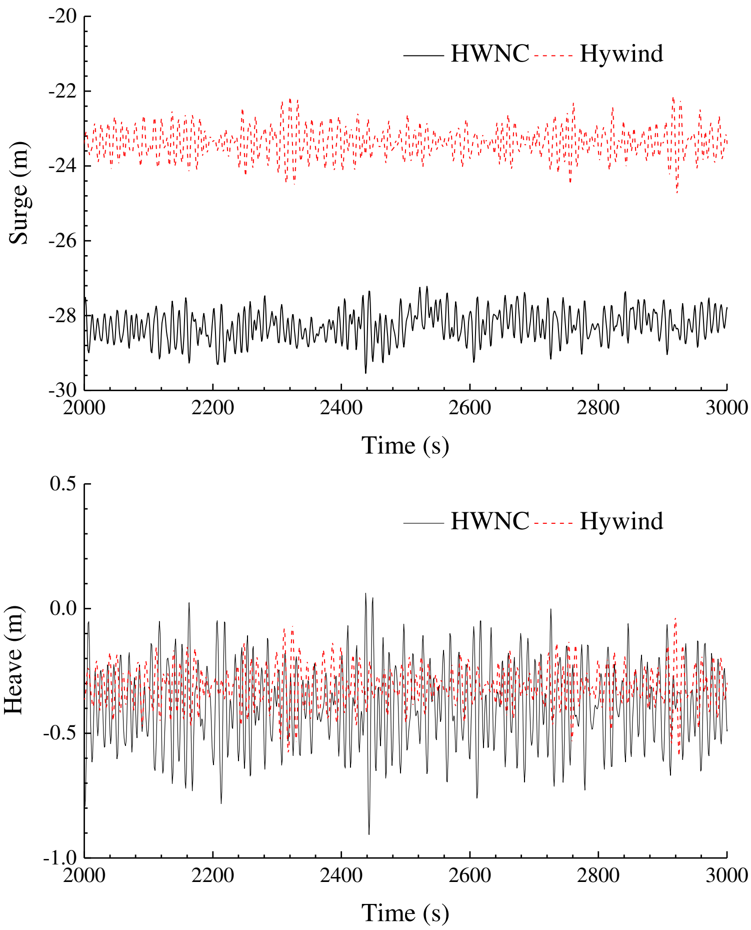


Fig. 12. Time series of platform motions, LC2.

Table 5
Statistical results of platform motions, LC2.

| | | Max | Min | Mean | Std. dev |
|---|---|---|---|---|---|
| HWNC | Surge (m) | -26.96 | -30.85 | -28.31 | 0.44 |
| | Heave (m) | 0.11 | -0.91 | -0.39 | 0.15 |
| | Ptich (deg) | -3.20 | -4.23 | -3.91 | 0.15 |
| Hywind | Surge (m) | -21.01 | -26.15 | -23.37 | 0.51 |
| | Heave (m) | -0.03 | -0.59 | -0.31 | 0.08 |
| | Pitch (deg) | -3.18 | -4.45 | -3.79 | 0.18 |

The reduction of surge and pitch motions can be attributed to the tidal turbines, which produce damping force. Considering that the sea current propagates along negative X direction, the thrust force acting on the tidal turbine can be approximated by

$$\mathrm{T}(\dot{\mathrm{x}}) = -\mathrm{C_T} \cdot \frac{1}{2}\rho\pi \mathrm{R}^2(\mathrm{u}+\dot{\mathrm{x}})^2 \tag{12}$$

where $C_T$ is the steady thrust force coefficient, u is the sea current speed, $\dot{x}$ is velocity of the tidal turbine along X direction. Applying Taylor expansion at $\dot{x} = 0$, the following series is derived

$$\mathrm{T}(\Delta\dot{\mathrm{x}}+0) = \mathrm{T}(0) - \mathrm{C_T}\rho\pi \mathrm{R}^2\mathrm{u}\Delta\dot{\mathrm{x}} - \mathrm{C_T}\rho\pi \mathrm{R}^2\mathrm{u}\Delta\dot{\mathrm{x}}^2 + \mathrm{O}(\Delta\dot{\mathrm{x}}^2) \tag{13}$$

The first term on the right side is a constant component, which only influences the mean position of the platform. The constant component also has an influence on the extreme response, which will be discussed in the following part of this paper. The third term is of second-order and can be regarded as a small component compared to the first-order term. The second term is a damping component which helps to reduce the platform motions.

The amplified heave motion is caused by the WEC. As shown in Fig. 13, the vertical wave excitation force acting on the spar platform is very limited considering the geometry of the spar buoy. Comparatively, the WEC is subjected to much larger vertical excitations since the water plane area of the WEC is 3.4 times that of the spar buoy. The vertical excitations will transfer to the spar buoy through the PTO facility and therefore the mooring lines will be excited significantly. The increased vertical excitation force is a negative effect produced by the WEC, which leads to worse dynamic response of the mooring lines.

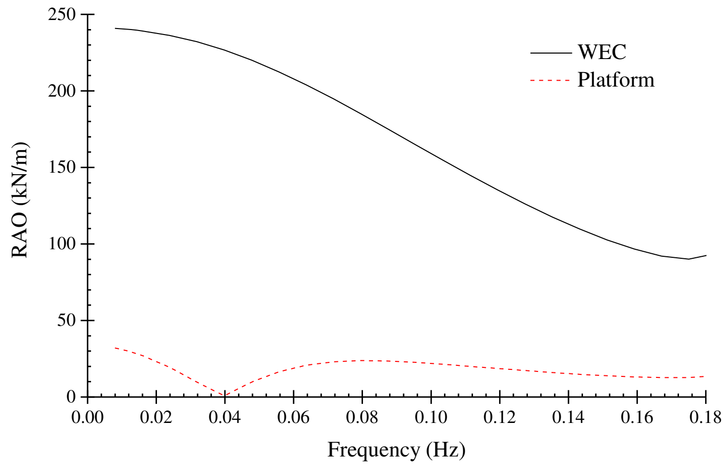


Fig. 13. RAO of vertical wave excitation force.

## 6.2. Structural responses

Fig. 14 shows the mean value and standard deviation of tower base fore-aft bending moment of the HWNC and the Hywind. It is found that the mean fore-aft bending moments of the two systems are nearly identical regardless of the environmental conditions. The good agreement between the two curves are not unexpected as the mean fore-aft bending moment at tower base is mainly produced by the thrust force acting on the wind turbine. It explains why the mean fore-aft bending moment does not increase from LC1 to LC6 although the wave condition becomes increasingly severe. Although the HWNC is subjected to an additional pitch moment produced by the tidal turbines, this extra component is undertaken by the mooring system and the hydrostatic restoring force. Moreover, the HWNC gives a smaller standard deviation than the Hywind in both below-rated and over-rated operational conditions.

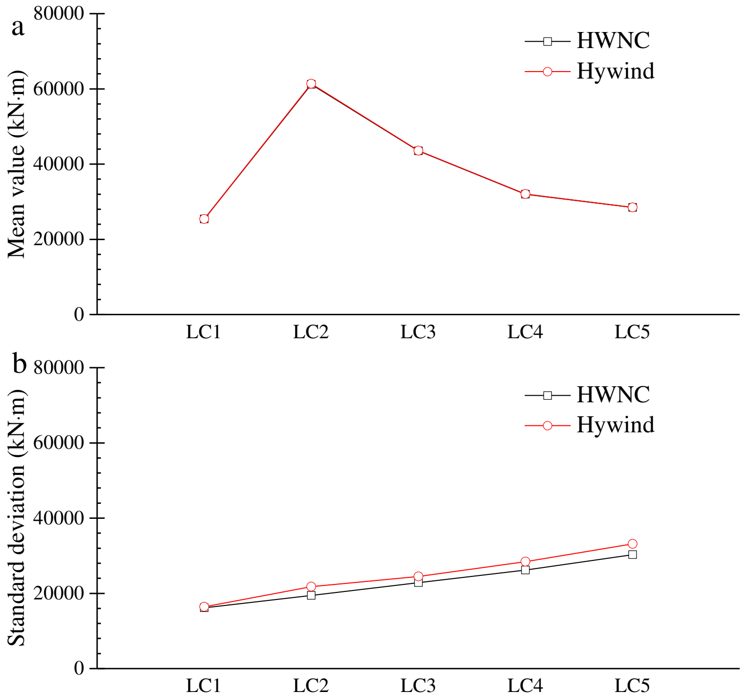


Fig. 14. Statistical results of tower base bending moment. (a) mean value; (b) standard deviation.

To further demonstrate the dynamic response of tower base, the time series of fore-aft bending moment is analysed with fast Fourier transform (FFT) method to acquire the power spectrum which is shown in Fig. 15. The majority of response energy concentrates within the wave frequency range and the response peak is observed at 0.09 Hz, which is close to the peak period of the stochastic waves. The HWNC generally gives a smaller response than the Hywind across the wave frequency range.

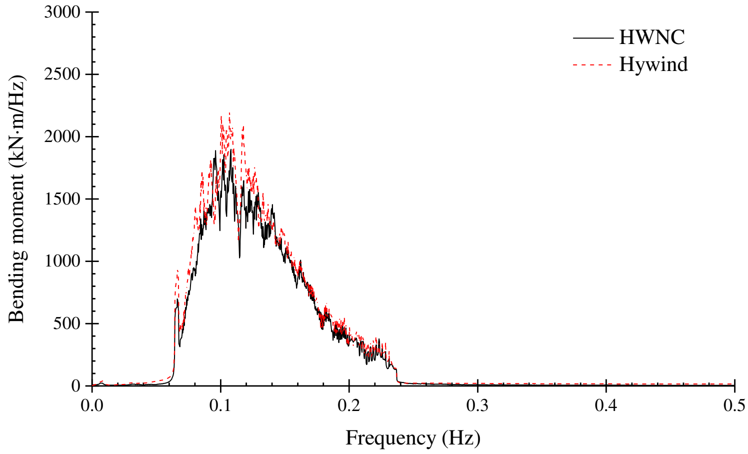


Fig. 15. FFT analysis results of tower base fore-aft bending moment, LC2.

Apart from the tower base fore-aft bending moment, the tension force of mooring line_1 is selected as another representation of the structural responses of the HWNC. Fig. 16 displays the time series of mooring line tension force in LC1. As shown, the mean value of the HWNC is larger than that of the Hywind. Statistics of the mooring line tension in other load cases are shown in Fig. 17. The mean mooring line tension forces of the two systems exhibit identical variation trend, which is very like that of the mean fore-aft bending moment. In fact, both the mean mooring tension force and the mean fore-aft bending moment is governed by the wind force whereas the wave force merely dominates the fluctuation. Nevertheless, a constant gap exists between the HNWC and the Hywind due to the thrust force acting on the tidal turbines.

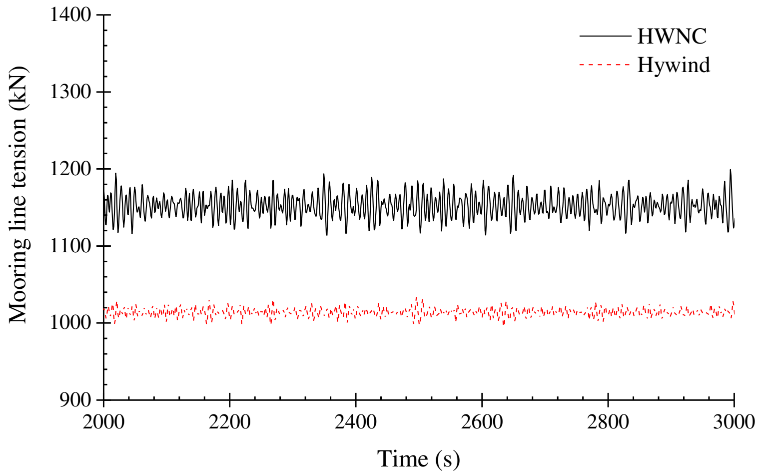


Fig. 16. Time series of line_1 tension force, LC1.

In spite of the reduced tower base fore-aft bending moment, the mooring line tension of the HWNC is substantially increased. Although the tidal turbine can produce damping forces, the constant component also brings more loads to the mooring system. Besides, the HWNC suffers additional vertical wave excitation forces.

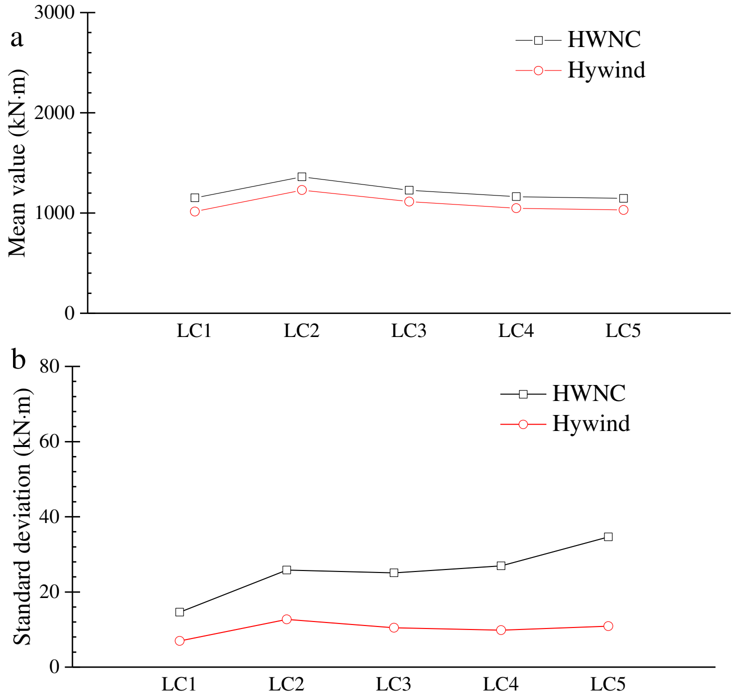


Fig. 17. Statistical results of line_1 tension force. (a) mean value; (b) standard deviation.

## 6.3. Extreme structural response

The 1-hr extreme values of tower base fore-aft bending moment and mooring line tension force are predicted based on the extrapolation method presented in Section 3.2. Fig. 18 shows the extrapolated up-crossing rate of the tower base fore-aft bending moment. Regardless of the environmental conditions, the up-crossing rate of the HWNC is generally lower than that of the Hywind at a given level $y_0$. According to Eq. (2), it implies that the fore-aft bending moment of the HWNC has a smaller probability to exceeds $y_0$. The level corresponding to up-crossing rate of $10^{-5}$ is selected in this study to represent the extreme values.

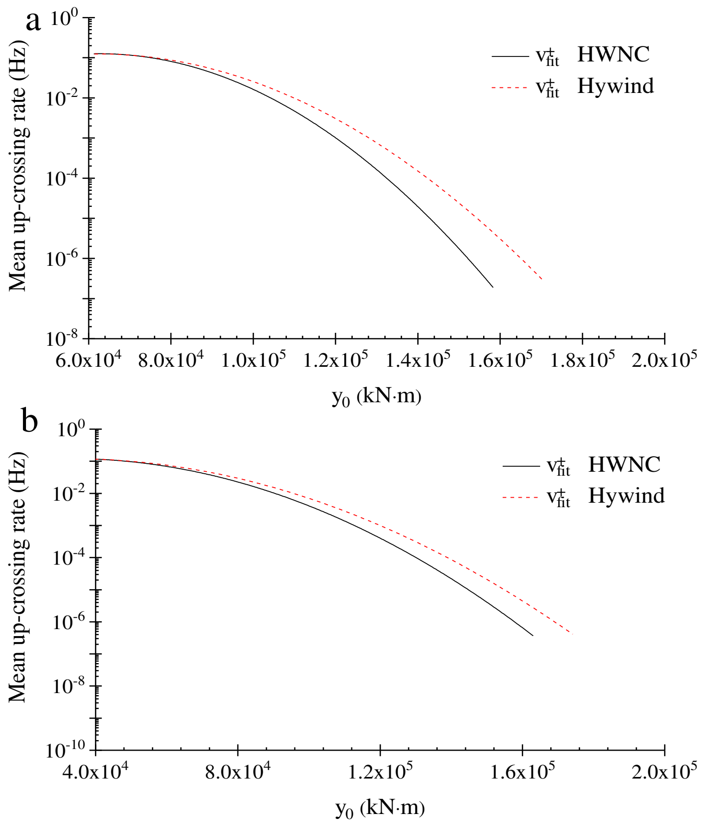


Fig. 18. Extrapolated up-crossing rate of tower base fore-aft bending moment (a) simulation case LC2; (b) simulation case LC4.

The extreme tower base fore-aft bending moments of the HWNC and the Hywind are demonstrated in Fig. 19. Generally, the extreme fore-aft bending moment is monotonic and it increases as the sea waves become severe. Nevertheless, the extreme value in simulation case LC2 reaches a relatively high level despite that the sea waves are moderate. According to the environmental conditions in Table 4, the wind thrust force is the largest in LC2 (the wind speed is closed to the rated value 11. 4 m/s in LC2), which induces a substantial fore-aft bending moment at the tower base and it is why the mean fore-aft bending moment is the largest in LC2. Therefore, the extreme fore-aft bending moment can still reach a very high level even if the sea waves are moderate. Although the wind turbine is parked and the system is subjected to no wind force in LC6, the extreme fore-aft bending moment is still the largest in all simulation cases due to the rare sea waves. Moreover, the HWNC gives a smaller extreme value than the Hywind. Considering that the fore-aft bending moment produced by the wind force is identical for the two systems, it can be deduced that the smaller extreme response of the HWNC is mainly attributed to the reduced pitch motion (see Fig. 20).

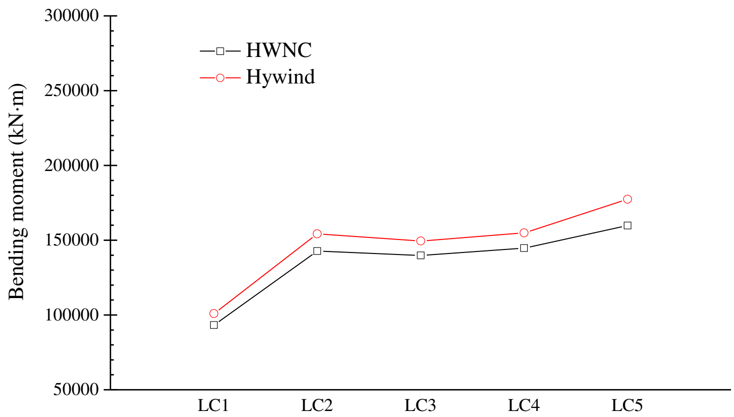


Fig. 19. Extreme tower base fore-aft bending moment.

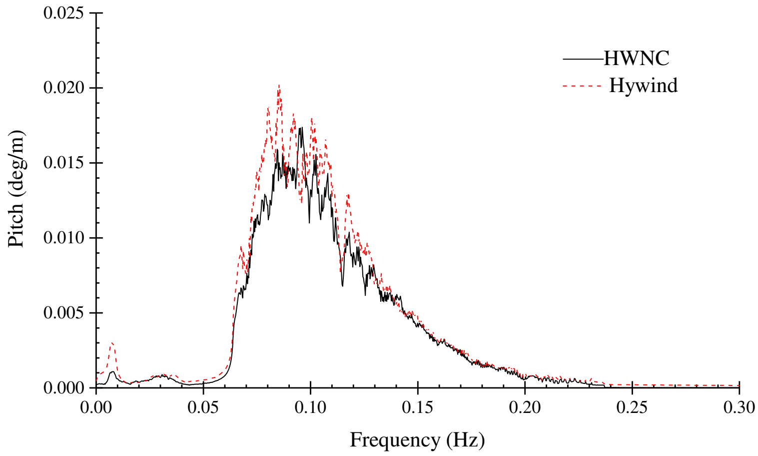


Fig. 20. Spectrum density of pitch motion, LC2.

Fig. 21 presents the extreme values of the mooring line tension force. The maximum mooring tension seems to be dominated by the wind force while the sea wave effect is limited. The maximum value does not increase with the significant wave height. Instead, the maximum mooring tension and the wind force have a similar variation trend. It implies that the critical condition for the mooring line is the rated operational condition rather than the extreme sea condition.

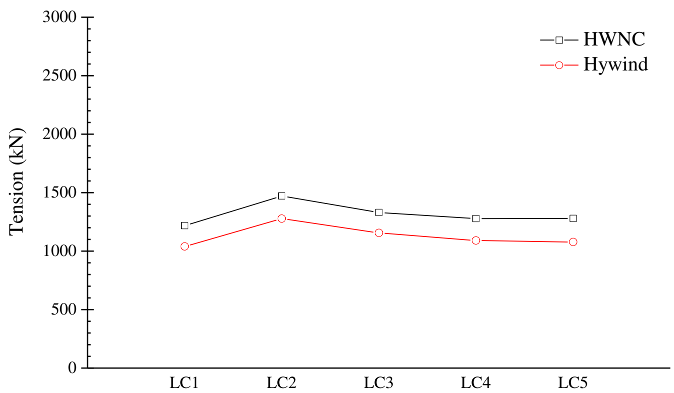


Fig. 21. Extreme mooring line tension force.

Despite the reduced maximum tower base fore-aft bending moment, the HWNC gives a worse extreme mooring tension. It is obviously a negative aspect produced by the installation of the WEC and the tidal turbines. The first item expands the fluctuation range of mooring line tension whereas the second term increases the average tension. Nevertheless, it should be noted that the wind and the sea current are aligned in the above simulation cases, which is the most unfavourable scenario for the HWNC. If the wind and the sea current propagate along opposite directions, the thrust forces acting on the wind turbine and the tidal turbines will offset each other, leading to a reduced extreme mooring tension. Fig. 22 shows the fitted up-crossing rate of the mooring tension when the sea current propagates along positive X axial. Due to the change of sea current propagation direction, the extreme mooring tension is significantly reduced. It indicates that the tidal turbine can play either a positive role or a negative role depending on the wave-current misalignment.

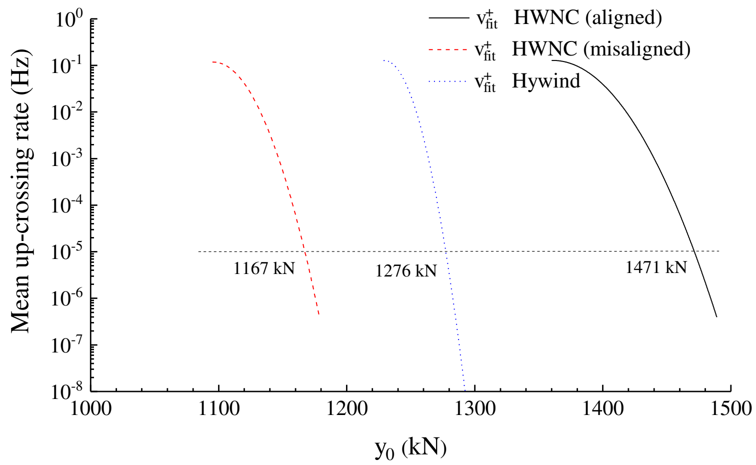


Fig. 22. Extrapolated mean up-crossing rate of mooring line tension force, LC2.

## 6.4. Fatigue damage calculation

The fatigue analysis is represented with the damage rate discussed in Section 3.3. The tower base fore-aft bending moment and the tension force of line_1 are considered here.

Fig. 23 displays the short-term fatigue damage rate of the tower base fore-aft bending moment. The damage rates of the two systems both increase when the sea wave becomes severe. Generally, the HWNC gives a lower damage rate than the Hywind. For example, the damage rate of the HWNC in LC2 is $9.63\times10^{-6}$ Hz, approximately 30% lower than that of the Hywind ($1.36\times10^{-5}$ Hz). Nevertheless, the discrepancies are less notable in LC1 and LC4. According to the results presented in Fig. 14(b), the fluctuation range of tower base fore-aft bending moment is narrowed due to installation of the WEC and the tidal turbines, which contributes to the reduced fatigue damage loads suffered by the HWNC.

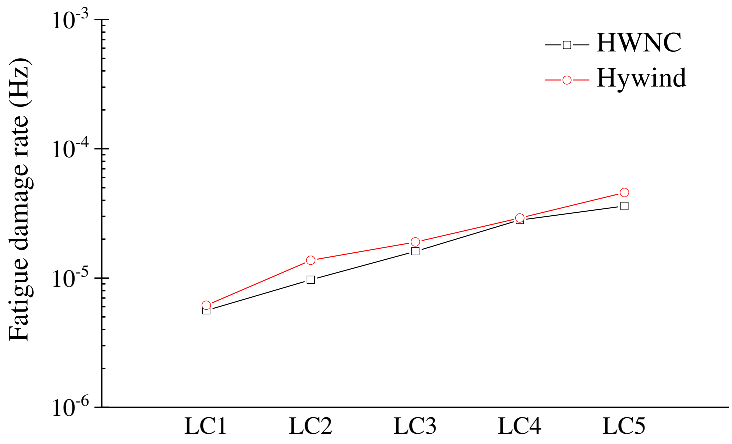


Fig. 23. Short-term damage rate of tower base fore-aft bending moment.

The fatigue damage rate of mooring tension is presented in Fig. 24. The contribution of WEC and tidal turbines to the fatigue damage rate is notable. Due to the thrust force acting on the tidal turbines, the mooring line will bear more loads to sustain the spar buoy. Also, the HWNC is subjected to much larger vertical wave excitation force and variation range of mooring line tension increase accordingly. The two factors together enhance the fatigue damage rate of the mooring line tension. The damage rate reaches a very high level in LC2, which is applicable to both the HWNC and the Hywind. It implies that the wind force has a dominating influence on the mooring line fatigue load.

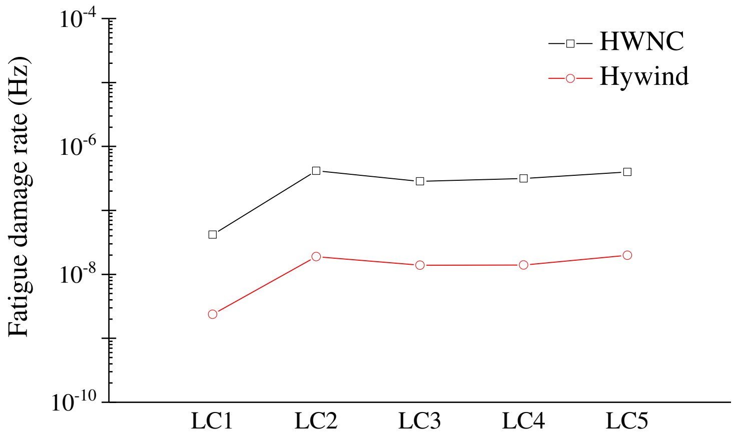


Fig. 24. Short-term damage rate of mooring line tension force.

According to Fig. 24, the fatigue damage rate shows observable discrepancies between the HWNC and the Hywind due to the thrust forces acting on the tidal turbines. To investigate the sensitivity of fatigue damage rate to the tidal turbine forces, the current speed in LC2 is varied. Table 6 lists the fatigue damage rate of mooring line tension when the HWNC is subject to various current speeds. As expected, the current speed (or tidal turbine force) has a negative effect on the mooring line since the mooring line will bear more loads to sustain the platform in the case of high current speed.

Table 6
Sensitivity of mooring tension fatigue damage rate to current speed

| | 1.0 m/s | 1.1 m/s | 1.2 m/s |
|---|---|---|---|
| Fatigue damage rate (Hz) | $4.2\times10^{-7}$ | $4.6\times10^{-7}$ | $5.9\times10^{-7}$ |

# 7. Conclusions

The structural responses of an integrated wind, wave and tidal energy system are addressed in this study. The integrated system is based on the combination of a spar type floating wind turbine, a point oscillating WEC and two tidal turbines. The mean up-crossing method is used to predict the extreme values of the stochastic responses. The size of simulation realizations is reduced by an extrapolation method, which approximates the up-crossing rate in tail region. The cumulative fatigue damage rate is calculated based on the S-N method. A comparative study between the integrated system and a spar type floating wind turbine is conducted to illustrate how the installation of the WEC and the tidal turbines influences the dynamic performance.

The stochastic responses of tower base fore-aft bending moment and mooring line tension force under a set of environmental conditions are simulated. It is favourable to see that the fore-aft bending moment are reduced as a result of the damping force produced by the tidal turbines. Nevertheless, the extra vertical wave excitation force acting on the WEC increases the response of mooring line substantially. A possible solution to this problem is adjustment of the PTO parameters, namely the stiffness coefficient K and the damping coefficient B. An appropriate configuration of the two parameters may help to relieve the problem or even eliminate it.

Based on the extrapolated up-crossing rate, the extreme values of the stochastic responses are estimated. Owing to the damping forces produced by the tidal turbines, the maximum fore-aft bending moment of the HWNC is smaller than that of the Hywind. It is an advantage of the HWNC. Nevertheless, the HWNC gives an extraordinary higher maximum mooring tension due to the thrust force acting on the tidal turbines. It should be noted that the wind and the sea current are set to propagate along the same direction in this study, which is the most dangerous scenario for the HWNC. An extra simulation shows that the maximum mooring tension of the HWNC can be reduced and even lower than that of the Hywind when the direction of sea current changes.

The cumulative damage rate is used to indicate the short-term fatigue damage caused to the structural component. It is shown that the tower base has a smaller probability to fail when the WEC and the tidal turbines are installed. On the contrary, the mooring line is subjected to higher damage loads.

# 8. Future work

A limitation of the current study is that wave-current couplings and wind turbulence are not considered. Future work aims to include the two factors in the numerical modelling to predict the performance of the HWNC in the natural world more accurately.

# Acknowledgment

The authors would like to acknowledge China Scholarship Council for the financial support (No. 201506230127).

# References

[1] F.G. Nielsen, T.D. Hanson, B. Skaare, Integrated dynamic analysis of floating offshore wind turbines, 25th International Conference on Offshore Mechanics and Arctic Engineering, American Society of Mechanical Engineers, 2006, pp. 671-679.

[2] Principle Power, 2017. http://www.principlepowerinc.com/.

[3] L. Li, Z. Hu, J. Wang, Q. Hu, Dynamic Responses of a Semi-type Offshore Floating Wind Turbine, ASME 2014 33rd International Conference on Ocean, Offshore and Arctic Engineering, American Society of Mechanical Engineers, 2014.

[4] L. Li, Z.Q. Hu, J. Wang, Y. Ma, Development and Validation of an Aero-hydro Simulation Code for Offshore Floating Wind Turbine, J Ocean Wind Energy 2(1) (2015) 1-11.

[5] Z.Q. Hu, L. Li, J. Wang, Q.H. Hu, M.C. Shen, Dynamic responses of a semi-type offshore floating wind turbine during normal state and emergency shutdown, China Ocean Eng 30(1) (2016) 97-112.

[6] F. Duan, Z. Hu, J. Wang, Model Tests of a Spar-Type Floating Wind Turbine Under Wind/Wave Loads, ASME 2015 34th International Conference on Ocean, Offshore and Arctic Engineering, American Society of Mechanical Engineers, 2015.

[7] Z.S. Cheng, H.A. Madsen, Z. Gao, T. Moan, A fully coupled method for numerical modeling and dynamic analysis of floating vertical axis wind turbines, Renew Energ 107 (2017) 604-619.

[8] L. Li, Y. Gao, Z. Hu, Z. Yuan, S. Day, H. Li, Model test research of a semisubmersible floating wind turbine with an improved deficient thrust force correction approach, Renew Energ 119 (2018) 95-105.

[9] X.T. Zhang, J.M. Yang, Power capture performance of an oscillating-body WEC with nonlinear snap through PTO systems in irregular waves, Appl. Ocean Res 52 (2015) 261-273.

[10] A. Elhanafi, G. Macfarlane, A. Fleming, Z. Leong, Experimental and numerical investigations on the hydrodynamic performance of a floating moored oscillating water column wave energy converter, Appl Energ 205 (2017) 369-390.

[11] D.Z. Ning, R.Q. Wang, Q.P. Zou, B. Teng, An experimental investigation of hydrodynamics of a fixed OWC Wave Energy Converter, Appl Energ 168 (2016) 636-648.

[12] Y.L. Chen, B.L. Lin, J. Lin, S.J. Wang, Experimental study of wake structure behind a horizontal axis tidal stream turbine, Appl Energ 196 (2017) 82-96.

[13] O.A. Lo Brutto, J. Thiébot, S.S. Guillou, H. Gualous, A semi-analytic method to optimize tidal farm layouts – Application to the Alderney Race (Raz Blanchard), France, Appl Energ 183 (2016) 1168-1180.

[14] A. Aubault, M. Alves, A. Sarmento, D. Roddier, A. Peiffer, Modeling of an oscillating water column on the floating foundation WindFloat, International Conference on Ocean, Offshore and Arctic Engineering, American Society of Mechanical Engineers, 2011, pp. 235-246.

[15] M.J. Muliawan, M. Karimirad, T. Moan, Dynamic response and power performance of a combined Spar-type floating wind turbine and coaxial floating wave energy converter, Renew Energ 50 (2013) 47-57.

[16] L. Wan, Z. Gao, T. Moan, Experimental and numerical study of hydrodynamic responses of a combined wind and wave energy converter concept in survival modes, Coast. Eng 104 (2015) 151-169.

[17] C. Michailides, C. Luan, Z. Gao, T. Moan, Effect of flap type wave energy converters on the response of a semi-submersible wind turbine in operational conditions, International Conference on Ocean, Offshore and Arctic Engineering, American Society of Mechanical Engineers, 2014, pp. V09BT09A014-V09BT09A014.

[18] L. Li, Y. Gao, Z.M. Yuan, S. Day, Z.Q. Hu, Dynamic response and power production of a floating integrated wind, wave and tidal energy system, Renew Energ 116 (2018) 412-422.

[19] E.E. Bachynski, T. Moan, Point absorber design for a combined wind and wave energy converter on a tension-leg support structure, International Conference on Ocean, Offshore and Arctic Engineering, American Society of Mechanical Engineers, 2013, pp. V008T09A025-V008T09A025.

[20] Z.S. Cheng, H.A. Madsen, W. Chai, Z. Gao, T. Moan, A comparison of extreme structural responses and fatigue damage of semi-submersible type floating horizontal and vertical axis wind turbines, Renew Energ 108 (2017) 207-219.

[21] Z.Q. Hu, Y. Liu, J. Wang, An integrated structural strength analysis method for Spar type floating wind turbine, China Ocean Eng 30(2) (2016) 217-230.

[22] Q.Y. Li, Z. Gao, T. Moan, Modified environmental contour method for predicting long-term extreme responses of bottom-fixed offshore wind turbines, Mar Struct 48 (2016) 15-32.

[23] C. Michailides, Z. Gao, T. Moan, Experimental and numerical study of the response of the offshore combined wind/wave energy concept SFC in extreme environmental conditions, Mar Struct 50 (2016) 35-54.

[24] X. Liu, C. Lu, G.Q. Li, A. Godbole, Y. Chen, Effects of aerodynamic damping on the tower load of offshore horizontal axis wind turbines, Appl Energ 204 (2017) 1101-1114.

[25] N. Aggarwal, R. Manikandan, N. Saha, Nonlinear short term extreme response of spar type floating offshore wind turbines, Ocean Eng 130 (2017) 199-209.

[26] H.R. Li, Z.Q. Hu, J. Wang, X.Y. Meng, Short-term fatigue analysis for tower base of a spar-type wind turbine under stochastic wind-wave loads, International Journal of Naval Architecture and Ocean Engineering (2017).

[27] E. Marino, A. Giusti, L. Manuel, Offshore wind turbine fatigue loads: The influence of alternative wave modeling for different turbulent and mean winds, Renew Energ 102 (2017) 157-169.

[28] P.A. Graf, G. Stewart, M. Lackner, K. Dykes, P. Veers, High-throughput computation and the applicability of Monte Carlo integration in fatigue load estimation of floating offshore wind turbines, Wind Energy 19(5) (2016) 861-872.

[29] J.M. Jonkman, Definition of the Floating System for Phase IV of OC3, Citeseer2010.

[30] NWTC Information Portal. (WEC-Sim), 2017. https://nwtc.nrel.gov/WEC-Sim. (Accessed 15-September 2017).

[31] A.R. Bramwell, D. Balmford, G. Done, Bramwell's helicopter dynamics, Butterworth-Heinemann2001.

[32] A. Naess, T. Moan, Stochastic dynamics of marine structures, Cambridge University Press2012.

[33] A. Naess, O. Gaidai, Monte Carlo methods for estimating the extreme response of dynamical systems, J Eng Mech-Asce 134(8) (2008) 628-636.

[34] NWTC Information Portal, 2017. https://nwtc.nrel.gov/MLife. (Accessed 15-September 2017).

[35] D.N. Veritas, Fatigue design of offshore steel structures, No. DNV-RP-C203, 2010.

[36] J.M. Jonkman, S. Butterfield, W. Musial, G. Scott, Definition of a 5-MW reference wind turbine for offshore system development, National Renewable Energy Laboratory Golden, CO, 2009.

[37] J.M. Jonkman, M.L. Buhl Jr, FAST User's Guide, National Renewable Energy Laboratory (NREL), 2005.

[38] B.J. Koo, A.J. Goupee, R.W. Kimball, K.F. Lambrakos, Model Tests for a Floating Wind Turbine on Three Different Floaters, J Offshore Mech Arct 136(2) (2014) 020907.

[39] K. Johannessen, T.S. Meling, S. Hayer, Joint distribution for wind and waves in the northern north sea, The Eleventh International Offshore and Polar Engineering Conference, International Society of Offshore and Polar Engineers, 2001.

[40] IEC, International Standard 61400-3, Wind Turbines, Part 3: Design Requirements for Offshore Wind Turbines,, 2009.

[41] O.M. Faltinsen, Sea Loads on Ships and Offshore Structures, Cambridge University Press1993.